Superconductivity from repulsive interactions in Bernal-stacked bilayer graphene

Glenn Wagner,[1] Yves H. Kwan,[2,3] Nick Bultinck,[2,4] Steven H. Simon,[2] and S.A. Parameswaran[2]

[1] *Department of Physics, University of Zurich, Winterthurerstrasse 190, 8057 Zurich, Switzerland*
[2] *Rudolf Peierls Centre for Theoretical Physics, Parks Road, Oxford, OX1 3PU, UK*
[3] *Princeton Center for Theoretical Science, Princeton University, Princeton NJ 08544, USA*
[4] *Department of Physics, Ghent University, Krijgslaan 281, 9000 Gent, Belgium*

A striking series of experiments have observed superconductivity in Bernal-stacked bilayer graphene (BBG) when the energy bands are flattened by applying an electrical displacement field. Intriguingly, superconductivity manifests only at non-zero magnetic fields, or when spin-orbit coupling is induced in BBG by coupling to a substrate. We present detailed functional renormalization group and random-phase approximation calculations that provide a unified explanation for the superconducting mechanism in both cases. Both calculations yield a purely electronic p-wave instability of the Kohn-Luttinger (KL) type. The latter can be enhanced either by magnetic fields or Ising spin-orbit coupling, naturally explaining the behaviour seen in experiments.

Introduction.—The explosion of interest in magic-angle twisted bilayer graphene (TBG), sparked by experimental observations of gate-tunable superconductivity (SC) [1–4] and correlated insulating behaviour [1, 3–20], has stimulated broader investigations of correlated electron physics in two-dimensional materials with narrow energy bands. Recently, several systems of moiréless graphene multilayers have been shown to host correlation effects reminiscent of their more complex cousins. Most notably, the application of an electrical displacement field to Bernal-stacked bilayer graphene (BBG) and rhombohedral trilayer graphene (RTG) flattens the bands near neutrality and gate-tunable SC has been observed in both BBG [21–25], RTG [26–28] and tetralayer graphene [29] in such a setting. In the phase diagram of both systems, the superconductor is proximate to a cascade of symmetry-breaking transitions, again a feature familiar from TBG.

Experimentally, RTG exhibits a cascade of symmetry-breaking transitions and SC with a critical temperature $T_c = 106$ mK. As in TBG, the symmetry-breaking transitions can be explained within a Hartree-Fock mean-field approximation [30], while candidate theories of SC in RTG range from purely electronic mechanisms [31–39] to acoustic-phonon-mediated attraction [40].

Similar to TBG and RTG, quantum oscillation measurements in BBG show a variety of isospin symmetry breaking transitions [41, 42], that can be understood in terms of Stoner ferromagnetism [43, 44]. In contrast to those systems, however, BBG becomes superconducting only in the presence of either an in-plane magnetic field [21] or spin-orbit coupling (SOC) induced by placing the BBG on top of a layer of WSe_2 [22], with transition temperatures of $T_c = 26$ mK and $T_c = 260$ mK respectively. Although both phonon-mediated [40, 45, 46] and purely electronic SC mechanisms have been proposed for BBG [39, 43, 44, 47, 48], the requirement of a magnetic field or SOC to trigger SC is a new ingredient, absent in either TBG or RTG, that could help pinpoint the nature of the SC instability. A possible explanation based on fluctuating superconductivity was proposed in Ref. [49], which remained agnostic as to the origin of the pairing "glue".

A Kohn-Luttinger mechanism provides a potential pathway for superconductivity from purely repulsive interactions, by generating an effective interaction in higher angular momentum channels via overscreening of the Coulomb interaction [50], yet its viability and the precise features of the resulting SC will depend sensitively on details of the underlying Fermi liquid parent state. Kohn-Luttinger mechanisms have been proposed for TBG [51, 52], RTG [31, 32, 34, 35, 37–39, 53, 54] and BBG [39, 43, 44, 47, 48, 54]. In our work we study Kohn-Luttinger type SC in BBG via the random-phase approximation (RPA) and functional renormalization group (FRG) calculations. The results from both approaches can be described within a simplified three-pocket model that captures the essential features of the BBG Fermi surface. By incorporating the effects of applied field and SOC, we show that an all-electronic superconducting mechanism provides a unified explanation for both classes of experiment.

Hamiltonian.— We begin with a low-energy four-band model for electrons in BBG [55, 56]. In the basis $\{1A, 1B, 2A, 2B\}$ (where the number indicates the layer and A/B label distinct sublattices in a single layer) the low-energy Hamiltonian is

$$H = \begin{pmatrix} \frac{D}{2} & v_0\pi^\dagger & -v_4\pi^\dagger & -v_3\pi \\ v_0\pi & \Delta' + \frac{D}{2} & t_1 & -v_4\pi^\dagger \\ -v_4\pi & t_1 & \Delta' - \frac{D}{2} & v_0\pi^\dagger \\ -v_3\pi^\dagger & -v_4\pi & v_0\pi & -\frac{D}{2} \end{pmatrix}, \quad (1)$$

where $\pi = \hbar(\tau_z k_x + i k_y)$ and s_i and τ_i denote Pauli matrices associated with spin and valley respectively. The displacement field is chosen to be $D = 50\,\text{meV}$ and $v_i = t_i\sqrt{3}a/2\hbar$ with $a = 0.246\,\text{nm}$ the lattice constant of graphene. We use the tight-binding parameters [56], $t_0 = 2.61\,\text{eV}$, $t_1 = 0.361\,\text{eV}$, $t_3 = 0.283\,\text{eV}$, $t_4 = 0.138\,\text{eV}$ and $\Delta' = 0.015\,\text{eV}$. t_3 controls the trigonal warping. We add the gate-screened Coulomb interaction $V^0(q) = \frac{e^2}{2\epsilon_0\epsilon_r q}\tanh q d_{\text{sc}}$ with screening length d_{sc} and

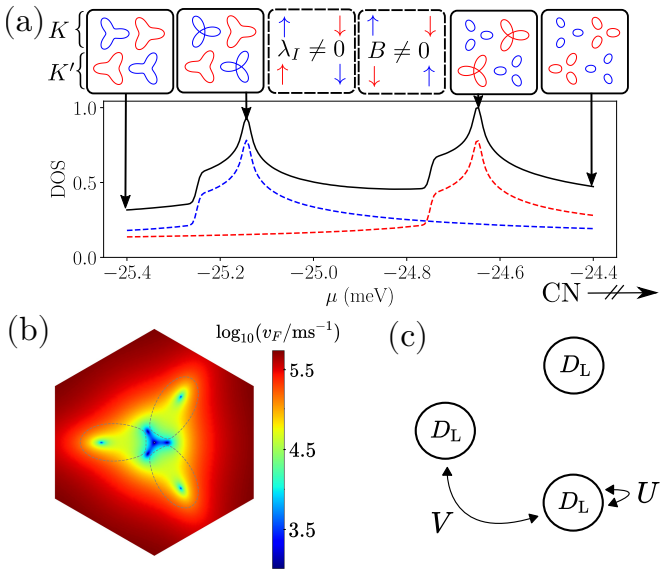

FIG. 1. (a) Density of states (DOS) as a function of the chemical potential μ in the presence of Ising SOC $\lambda_I = 0.5$meV or equivalently an in-plane field of $B = 4.3$T. Red and blue dashed lines are contributions of distinct symmetry-related Fermi surfaces (FSs) of the four spin/valley species shown in the solid boxes to the total DOS (black solid line). The B-field and Ising SOC lead to distinct assignments of spin labels to the FSs (dashed boxes). The vHS closer to charge neutrality (CN, $\mu = 0$) corresponds to the majority isospin species, whereas the one further from CN corresponds to the the minority isospin species. Strong SC is only observed near the former. We include thermal broadening of $T = 0.1$K. (b) Fermi velocity in the Brillouin zone close to the K-point with dashed FS for $B = 0$ and $\mu = -24.92$meV. (c) Pocket model derived from three pockets with inter-pocket (V) and intra-pocket (U) interactions.

relative permittivity ϵ_r. We choose a UV cutoff to more finely resolve details of the Fermi surface [57]. We neglect the Bloch form factors for simplicity; while the form factors may quantitatively impact the results [58], a quantitatively precise estimate of T_c is beyond the scope of our present study. We also neglect the weak intervalley exchange scattering, such that our model has separate spin rotation symmetry in each valley, i.e. $SU(2)_K \times SU(2)_{K'}$. In this limit, the magnetic field Zeeman term $\mu_B B_Z s_z$ and the Ising SOC term $\frac{\lambda_I}{2} s_z \tau_z$ are equivalent (up to a flavour rotation) and we can treat the SOC as an effective Zeeman field $B_{\rm SOC} = \lambda_I/(2\mu_B)$. In the presence of a Zeeman field the density of states of majority and minority isospin species exhibit van Hove singularities (vHS) at different chemical potentials (see Fig. 1).

Pocket model.— A key outcome of our detailed numerical simulations is that the key features of SC in BBG can be captured within a simplified three-pocket model, that we now describe to orient our discussion (and justify *a posteriori*, via our RPA/FRG calculations). The distinguishing feature of the Fermi surface shown in Fig. 1c is the presence of three pockets related by C_3 symmetry each with density of states D_L. Even in the case where the Fermi surface is simply connected, the density of states still has three sharp peaks around the lobes [59], motivating a three-pocket model. The key physics is then controlled by couplings U, V that represent the intra-pocket and inter-pocket interactions respectively. The gap equation takes the form $\sum_{\mathbf{k}'} M_{\mathbf{k},\mathbf{k}'} \Delta_{\mathbf{k}'} = \lambda \Delta_{\mathbf{k}}$, where $\mathbf{k}$ runs over N_p momenta lying on the Fermi surface. Assuming for now that the interactions are the same for all the momenta within one pocket, the gap matrix simplifies to a 3×3 matrix

$$M = -\begin{pmatrix} U & V & V \\ V & U & V \\ V & V & U \end{pmatrix}, \tag{2}$$

where we have neglected dimensional and normalization factors. A positive eigenvalue λ at a temperature scale E_0 set by the UV cutoff [59] indicates a superconducting instability (i.e. λ reaching unity) at a lower temperature $T_c \sim E_0 e^{-\frac{1}{\lambda}}$, assuming the cutoff E_0 is small enough that we are in the logarithmic temperature scaling regime. M has leading eigenvectors $\Delta \sim (1, e^{\pm\frac{2\pi i}{3}}, e^{\pm\frac{4\pi i}{3}})^T$ corresponding to a degenerate p-wave solution with eigenvalue $\lambda_p = (V - U)$. The bare Coulomb interaction is monotonically decreasing as a function of momentum and therefore at the bare level $V^0 < U^0$ and there is no superconductivity. However, due to screening we can have $V > U$ such that we obtain superconductivity. Within the RPA, screening leads to

$$\lambda_p = \frac{V^0}{1 + \Pi(q_P) V^0} - \frac{U^0}{1 + \Pi(0) U^0}, \tag{3}$$

where q_P is the inter-pocket distance, $\Pi(0)$ reflects the total DOS, and $\Pi(q_P)$ is roughly the average of the polarization function within the annular region in Fig. 2d. Since $\Pi(0) > \Pi(q_P)$, we can obtain $\lambda_p > 0$ after the screening.

RPA.— To demonstrate that a Kohn-Luttinger-like mechanism can lead to superconductivity in BBG, we perform an initial RPA analysis. An RPA analysis on BBG was already performed in [47], where nodal s-wave and p-wave solutions are obtained and SOC is seen to enhance the critical temperature. In our calculation we use a patching scheme that involves dividing the Fermi surface into finite segments, with the dispersion in the direction perpendicular to the Fermi surface treated in the linear approximation and integrated (with UV cutoff E_0) to obtain the logarithmic Cooper divergence. The largest positive eigenvalue λ of the the symmetrized gap matrix corresponds to a superconducting solution with $T_c \sim E_0 e^{-\frac{1}{\lambda}}$. The details of the RPA calculation are provided in [59].

Fig. 2a charts the maximum eigenvalue λ as a function of chemical potential and applied Zeeman field. Focusing first on $B = 0$, we find that superconductivity exists

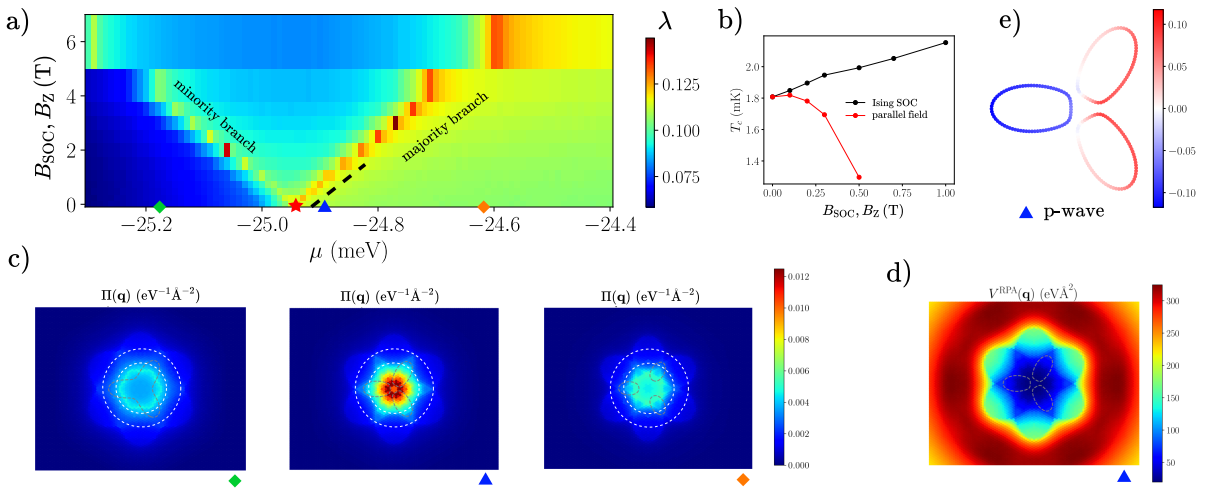

FIG. 2. **Kohn-Luttinger superconductivity in the random phase approximation. a)** Maximum gap matrix eigenvalue λ, related to the superconducting critical temperature $T_c \sim E_0 e^{-\frac{1}{\lambda}}$, as a function of Zeeman field B and chemical potential μ. **b)** Comparison of the effects of orbital coupling due to an in-plane magnetic field on T_c. Horizontal axis corresponds to the dotted black line in a). Energy cutoff of the gap equation set as $E_0 = 10\,\text{meV}$. **c)** Static polarization function in the absence of a (generalized) Zeeman field at three dopings indicated by the corresponding symbols in a). The annular region between the dashed white lines indicates the momentum range that contributes to $\Pi(q_P)$, where q_P is the inter-pocket momentum. **d)** RPA-screened interaction at the chemical potential indicated with a blue triangle in a). Bare interaction is of the dual gate-screened form with relative permittivity $\epsilon_r = 5$ and screening distance $d_{sc} = 38\,\text{nm}$ and we set $\Delta' = 0\text{meV}$. Fermi surface in valley $\tau = +$ is shown with grey dashed contours. **e)** Representative gap function corresponding to p-wave superconductivity. The solution is two-fold degenerate (we show the p_x solution).

for all values of μ shown, despite purely repulsive electronic interactions. The maximum T_c is attained around the vHS, which is expected since the high DOS both increases the strength of screening and the weighting in the gap equation. Indeed, the dependence of λ along the μ-axis echoes the salient features of the DOS (Fig. 1). The solution is predominantly the 2D irreducible representation corresponding to a p-wave gap function (Fig. 2e), though a non-degenerate extended s-wave solution — where the order parameter changes sign between the inner and outer parts of the Fermi surface — is competitive in a narrow sliver of doping at the vHS, especially for larger ϵ_r [59].

Moving to finite fields, we find that the T_c peak in Fig. 2a splits off into two branches which follow the vHS of the majority and minority spins. The spin projection involved in pairing remains at the van Hove filling, while the detuning of the opposite 'spectator' spin leads to a change in screening properties and hence λ_p. Naïvely, shifting the spectator spin away from the vHS would sharply reduce the DOS and suppress KL superconductivity. However, owing to the narrow dispersion, a small Zeeman shift significantly changes the Fermi surface, and hence the polarization function. Along the minority branch, the spectator Fermi surface expands and fills in the voids at the Dirac momenta, leading to a slight enhancement of $\Pi(q_P)$ (right panel of Fig. 2d). On the other hand for the majority branch, the Fermi surface shrinks into small pockets such that screening at q_P, which is deleterious to the superconductivity, is less effective (middle panel of Fig. 2d). [This saturates when the field fully polarizes the spins, which occurs at $B \gtrsim 10\,\text{T}$ for our parameters.] This therefore leads to a strongly asymmetric contribution from the first term in Eq. 3 and hence stronger pairing in the 'majority branch' (doping towards CN).

In the case of a physical magnetic field, even though $\boldsymbol{B}$ is actually applied parallel to the graphene sheets, the orbital coupling (enabled by the finite interlayer distance) may be non-negligible owing to the small energy scales involved. For $B \sim 1\,\text{T}$, the typical depairing energy $\epsilon_K(\boldsymbol{k}) - \epsilon_{K'}(-\boldsymbol{k})$ is of order 0.01 meV, which is comparable to T_c. Indeed, upon incorporating the orbital effects of the magnetic field in the gap equation [59], we find a substantial suppression in λ which may lead to a peak in T_c at a finite B (Fig. 2b). This effect is absent if the flavors are imbalanced instead by Ising spin-orbit coupling.

FRG.— We perform an FRG calculation in order to confirm that the superconductivity persists when fluctuations beyond the RPA are taken into account. FRG is a intermediate-coupling approach that involves integrating out high-energy degrees of freedom, in order to obtain a renormalized interaction valid close to the Fermi surface [60–66]. FRG has been used to study SC in both TBG [67–70] and RTG [37], yet has not to date been applied to biased BBG. The central object of the FRG

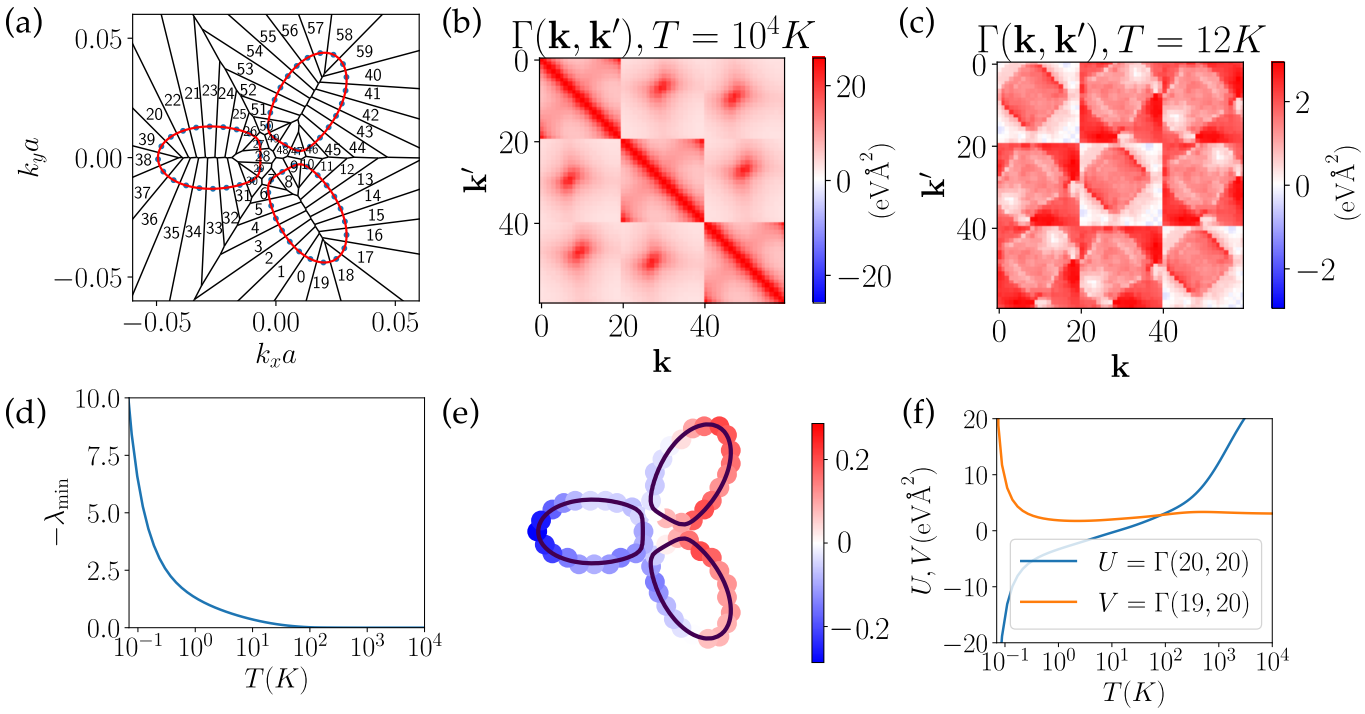

FIG. 3. **Superconductivity in a functional renormalization group calculation**. (a) Patching scheme of the majority spin Fermi surface with $N_p = 60$ patches for a chemical potential 0.05meV above the vHS. (b,c) BCS vertex $\Gamma(\mathbf{k},\mathbf{k}')$ at $T = 10^4$K, 12K respectively. Note that the value of $\Gamma(\mathbf{k},\mathbf{k}')$ depends on the size of the patches at $\mathbf{k}$ and $\mathbf{k}'$. The numbers refer to the patch labels defined in (a). We use the Coulomb interaction with $d_{\rm sc} = 25$nm and $\epsilon_r = 17.5$. (d) The divergence of the most negative eigenvalue of the superconducting susceptibility signifies the superconducting T_c. (e) The two-fold degenerate leading eigenvector of the gap equation is a p-wave order parameter. We show the p_x solution. (f) The flow of two components of the vertex representative of intra-pocket ($U = \Gamma(20,20)$) and inter-pocket ($V = \Gamma(19,20)$) scattering. The polarization bubbles are evaluated with $N_{\rm ref} = 101$.

calculation is the temperature-dependent 4-point vertex $\gamma_{ab;cd}(\boldsymbol{p}_1,\boldsymbol{p}_2,\boldsymbol{p}_3)$, where the composite subscripts $a, b, \ldots$ label both spin and valley. The FRG equations are [63]

$$\dot{\gamma}_{abcd}(\boldsymbol{p}_1,\boldsymbol{p}_2,\boldsymbol{p}_3) = \int_{\boldsymbol{k}} \sum_{xy} \frac{1}{2} \times \tag{4}$$
$$\Big[-\dot{\pi}^{pp}_{xy}(\boldsymbol{k}, \boldsymbol{p}_1+\boldsymbol{p}_2)\gamma_{abxy}(\boldsymbol{p}_1,\boldsymbol{p}_2,\boldsymbol{k})\gamma^*_{cdxy}(\boldsymbol{p}_3,\boldsymbol{p}_4,\boldsymbol{k})$$
$$+ 2\dot{\pi}^{ph}_{xy}(\boldsymbol{k}, \boldsymbol{p}_1-\boldsymbol{p}_3)\gamma^*_{cxay}(\boldsymbol{p}_3,\boldsymbol{k},\boldsymbol{p}_1)\gamma_{bxdy}(\boldsymbol{p}_2,\boldsymbol{k},\boldsymbol{p}_4)$$
$$- 2\dot{\pi}^{ph}_{xy}(\boldsymbol{k}, \boldsymbol{p}_2-\boldsymbol{p}_3)\gamma^*_{cxby}(\boldsymbol{p}_3,\boldsymbol{k},\boldsymbol{p}_2)\gamma_{axdy}(\boldsymbol{p}_1,\boldsymbol{k},\boldsymbol{p}_4)\Big],$$

where $\dot{} \equiv \partial_T$ (we employ the temperature-flow FRG scheme [63], where the RG scale is set by the temperature). The momentum arguments $\boldsymbol{p}_i$ of the 4-point vertex are chosen to be N_p equally spaced patch momenta on the Fermi surface (Fig. 3a). To capture the details of the bandstructure, we evaluate the polarization bubbles π^{pp} and π^{ph} on a fine $N_{\rm ref} \times N_{\rm ref}$ mesh [59]. We start the FRG flow at a temperature of 10^4K and flow down to 10^{-3}K in logarithmic steps. The temperature at which the superconducting susceptibility diverges defines the superconducting critical temperature T_c.

The Coulomb interaction is a monotonically decreasing function of momentum transfer and this sets the structure of the initial vertex: The maximum values of the vertex are attained for small intra-pocket momentum transfers or for small momentum transfers between points in different pockets close to the K-point (Fig. 3b). The gap matrix in Fig. 3b echoes the block structure of Eq. 2. We have $U > V$ and no superconducting instability. At lower temperatures, the bare interaction has been screened such that the components of the vertex with larger momentum transfers are larger than those with small momentum transfer (Fig. 3c), i.e. $V > U$ in Eq. (2). U is screened more heavily than V since $\Pi(0) > \Pi(q_P)$. In Fig. 3f we show the FRG flow of two representative components of the vertex function that show this screening behaviour as in Eq. (3). At the end of the FRG flow we have $V > U$ which leads to a divergence in the most negative eigenvalue of the superconducting susceptibility (Fig. 3d) in the p-wave channel (Fig. 3e) in agreement with both the pocket model and the RPA. However, in contrast to the RPA calculation, screening in the FRG can lead to $U < 0$, further enhancing the superconductivity. In the Supplement [59] we show that intervalley Coulomb scattering can also enhance the superconduc-

tivity, as was already shown in Ref. [48].

For the parameters $d_{\rm sc} = 25$nm and $\epsilon_r = 17.5$ we find $T_c \approx 0.5$K, which is larger than the experimentally observed value. However, since this is a nodal order parameter, disorder would reduce this scale. Possible sources of disorder include strain [71] and coupling to the substrate [72, 73], though the recent BBG devices are typically in an ultraclean regime. We caution that quantitative predictions of T_c from FRG calculations are challenging [37] and FRG may overestimate T_c [63].

Conclusions.—We have shown that a Kohn-Luttinger mechanism based on overscreening of an initially purely repulsive interaction provides a unified explanation for superconductivity in BBG either in the presence of a parallel magnetic field or SOC induced by proximity to WSe_2. The Kohn-Luttinger mechanism for parabolic bands in two dimensions is weak [31, 74, 75], however the deviations from parabolicity ('trigonal warping') in BBG as well as the imbalancing of the occupation numbers of the different isospin flavours due to an effective Zeeman field enhance the effect. Furthermore, the flat bands of BBG induced by the applied displacement field as well as the proximity to a van Hove singularity provide a high density of states, leading to a T_c in a realistic range. We find robust p-wave superconductivity in both RPA and FRG calculations, which lends support to a simplified three-pocket model. Intra-pocket interactions are more heavily screened than inter-pocket interactions, leading to an overall attraction in the p-wave channel. The details of the screening lead to enhanced superconductivity when doping towards charge neutrality as opposed to away from charge neutrality which is consistent with experimental observations. In the RPA calculation, we also find an extended s-wave solution [59]. Extending the existing STM studies on BBG to measure Andreev reflection [76] or performing quasiparticle interference experiments [77] could provide an experimental test to distinguish the p-wave or s-wave nature of the superconducting order parameter.

The Fermi surface of RTG with trigonal warping and an applied displacement field also consists of three separate pockets for a range of doping close to the van Hove singularity and therefore the Kohn-Luttinger mechanism described by our three-pocket model would likely result in superconductivity in that material too, as has been observed in experiments [26]. Indeed Ref. [47] showed that a Kohn-Luttinger mechanism can explain superconductivity in both BBG and RTG. The three-pocket model thus provides a unifying explanation for superconductivity in graphene multilayers, unlike theories of superconductivity in RTG based on the annular Fermi surface [31, 37] (although Ref. [31] also looked at the three-pocket regime). On the other hand, for twisted bilayer graphene, experiments [1–5, 8–12, 15, 16] as well as numerics [78, 79] show a single simply-connected Fermi surface per flavour, such that a different mechanism must be responsible for superconductivity, underscoring the different physics at play in moiréless vs. moiré graphene multilayers [80].

Recent experiments have observed superconductivity in twisted WSe_2 [81, 82] and a Kohn-Luttinger mechanism has been proposed in that case as well [83], hence Kohn-Luttinger superconductivity may extend beyond graphene-based systems.

Acknowledgements.— We thank the authors of [47] for valuable comments on an earlier version of this manuscript. We acknowledge funding from the European Research Council (ERC) under the European Union's Horizon 2020 research and innovation program via ERC-StG-Neupert-757867-PARATOP (GW) and ERC-StG-Parameswaran-804213-TMCS (YHK, SAP), the Royal Society via a University Research Fellowship (NB), and EPSRC Grant EP/S020527/1 (SHS). Statement of compliance with EPSRC policy framework on research data: This publication is theoretical work that does not require supporting research data.

[1] Y. Cao, V. Fatemi, A. Demir, S. Fang, S. L. Tomarken, J. Y. Luo, J. D. Sanchez-Yamagishi, K. Watanabe, T. Taniguchi, E. Kaxiras, R. C. Ashoori, and P. Jarillo-Herrero, Correlated insulator behaviour at half-filling in magic-angle graphene superlattices, Nature **556**, 80 (2018).

[2] Y. Cao, V. Fatemi, S. Fang, K. Watanabe, T. Taniguchi, E. Kaxiras, and P. Jarillo-Herrero, Unconventional superconductivity in magic-angle graphene superlattices, Nature **556**, 43 (2018).

[3] M. Yankowitz, S. Chen, H. Polshyn, Y. Zhang, K. Watanabe, T. Taniguchi, D. Graf, A. F. Young, and C. R. Dean, Tuning superconductivity in twisted bilayer graphene, Science **363**, 1059–1064 (2019).

[4] X. Lu, P. Stepanov, W. Yang, M. Xie, M. A. Aamir, I. Das, C. Urgell, K. Watanabe, T. Taniguchi, G. Zhang, A. Bachtold, A. H. MacDonald, and D. K. Efetov, Superconductors, orbital magnets and correlated states in magic-angle bilayer graphene, Nature **574**, 653 (2019).

[5] J. M. Park, Y. Cao, K. Watanabe, T. Taniguchi, and P. Jarillo-Herrero, Flavour hund's coupling, chern gaps and charge diffusivity in moiré graphene, Nature **592**, 43–48 (2021).

[6] Y. Cao, D. Rodan-Legrain, J. M. Park, N. F. Q. Yuan, K. Watanabe, T. Taniguchi, R. M. Fernandes, L. Fu, and P. Jarillo-Herrero, Nematicity and competing orders in superconducting magic-angle graphene, Science **372**, 264–271 (2021).

[7] X. Liu, Z. Wang, K. Watanabe, T. Taniguchi, O. Vafek, and J. Li, Tuning electron correlation in magic-angle twisted bilayer graphene using coulomb screening, Science **371**, 1261 (2021).

[8] A. L. Sharpe, E. J. Fox, A. W. Barnard, J. Finney, K. Watanabe, T. Taniguchi, M. A. Kastner, and D. Goldhaber-Gordon, Emergent ferromagnetism near three-quarters filling in twisted bilayer graphene, Science **365**, 605–608 (2019).

[9] M. Serlin, C. L. Tschirhart, H. Polshyn, Y. Zhang, J. Zhu, K. Watanabe, T. Taniguchi, L. Balents, and A. F. Young, Intrinsic quantized anomalous hall effect in a moiré heterostructure, Science **367**, 900 (2020).

[10] P. Stepanov, I. Das, X. Lu, A. Fahimniya, K. Watanabe, T. Taniguchi, F. H. L. Koppens, J. Lischner, L. Levitov, and D. K. Efetov, Untying the insulating and superconducting orders in magic-angle graphene, Nature **583**, 375–378 (2020).

[11] S. Wu, Z. Zhang, K. Watanabe, T. Taniguchi, and E. Y. Andrei, Chern insulators, van hove singularities and topological flat bands in magic-angle twisted bilayer graphene, Nature Materials **20**, 488–494 (2021).

[12] U. Zondiner, A. Rozen, D. Rodan-Legrain, Y. Cao, R. Queiroz, T. Taniguchi, K. Watanabe, Y. Oreg, F. von Oppen, A. Stern, and et al., Cascade of phase transitions and dirac revivals in magic-angle graphene, Nature **582**, 203–208 (2020).

[13] A. T. Pierce, Y. Xie, J. M. Park, E. Khalaf, S. H. Lee, Y. Cao, D. E. Parker, P. R. Forrester, S. Chen, K. Watanabe, T. Taniguchi, A. Vishwanath, P. Jarillo-Herrero, and A. Yacoby, Unconventional sequence of correlated chern insulators in magic-angle twisted bilayer graphene, Nature Physics **17**, 1210 (2021).

[14] H. Polshyn, M. Yankowitz, S. Chen, Y. Zhang, K. Watanabe, T. Taniguchi, C. R. Dean, and A. F. Young, Large linear-in-temperature resistivity in twisted bilayer graphene, Nature Physics **15**, 1011 (2019).

[15] A. Uri, S. Grover, Y. Cao, J. A. Crosse, K. Bagani, D. Rodan-Legrain, Y. Myasoedov, K. Watanabe, T. Taniguchi, P. Moon, *et al.*, Mapping the twist-angle disorder and landau levels in magic-angle graphene, Nature **581**, 47 (2020).

[16] Y. Saito, J. Ge, K. Watanabe, T. Taniguchi, and A. F. Young, Independent superconductors and correlated insulators in twisted bilayer graphene, Nature Physics **16**, 926 (2020).

[17] I. Das, X. Lu, J. Herzog-Arbeitman, Z.-D. Song, K. Watanabe, T. Taniguchi, B. A. Bernevig, and D. K. Efetov, Symmetry-broken chern insulators and rashba-like landau-level crossings in magic-angle bilayer graphene, Nature Physics **17**, 710 (2021).

[18] Y. Saito, F. Yang, J. Ge, X. Liu, T. Taniguchi, K. Watanabe, J. Li, E. Berg, and A. F. Young, Isospin pomeranchuk effect in twisted bilayer graphene, Nature **592**, 220 (2021).

[19] A. Rozen, J. M. Park, U. Zondiner, Y. Cao, D. Rodan-Legrain, T. Taniguchi, K. Watanabe, Y. Oreg, A. Stern, E. Berg, *et al.*, Entropic evidence for a pomeranchuk effect in magic-angle graphene, Nature **592**, 214 (2021).

[20] P. Stepanov, M. Xie, T. Taniguchi, K. Watanabe, X. Lu, A. H. MacDonald, B. A. Bernevig, and D. K. Efetov, Competing zero-field chern insulators in superconducting twisted bilayer graphene, Phys. Rev. Lett. **127**, 197701 (2021).

[21] H. Zhou, L. Holleis, Y. Saito, L. Cohen, W. Huynh, C. L. Patterson, F. Yang, T. Taniguchi, K. Watanabe, and A. F. Young, Isospin magnetism and spin-polarized superconductivity in bernal bilayer graphene, Science **375**, 774 (2022).

[22] Y. Zhang, R. Polski, A. Thomson, É. Lantagne-Hurtubise, C. Lewandowski, H. Zhou, K. Watanabe, T. Taniguchi, J. Alicea, and S. Nadj-Perge, Enhanced superconductivity in spin–orbit proximitized bilayer graphene, Nature **613**, 268 (2023).

[23] Y. Zhang, G. Shavit, H. Ma, Y. Han, K. Watanabe, T. Taniguchi, D. Hsieh, C. Lewandowski, F. von Oppen, Y. Oreg, and S. Nadj-Perge, Twist-programmable superconductivity in spin-orbit coupled bilayer graphene (2024), arXiv:2408.10335 [cond-mat.supr-con].

[24] C. Li, F. Xu, B. Li, J. Li, G. Li, K. Watanabe, T. Taniguchi, B. Tong, J. Shen, L. Lu, J. Jia, F. Wu, X. Liu, and T. Li, Tunable superconductivity in electron- and hole-doped bernal bilayer graphene, Nature **631**, 300 (2024).

[25] L. Holleis, C. L. Patterson, Y. Zhang, Y. Vituri, H. M. Yoo, H. Zhou, T. Taniguchi, K. Watanabe, E. Berg, S. Nadj-Perge, and A. F. Young, Nematicity and orbital depairing in superconducting bernal bilayer graphene with strong spin orbit coupling (2024), arXiv:2303.00742 [cond-mat.supr-con].

[26] H. Zhou, T. Xie, T. Taniguchi, K. Watanabe, and A. F. Young, Superconductivity in rhombohedral trilayer graphene, Nature **598**, 434 (2021).

[27] C. L. Patterson, O. I. Sheekey, T. B. Arp, L. F. W. Holleis, J. M. Koh, Y. Choi, T. Xie, S. Xu, E. Redekop, G. Babikyan, H. Zhou, X. Cheng, T. Taniguchi, K. Watanabe, C. Jin, E. Lantagne-Hurtubise, J. Alicea, and A. F. Young, Superconductivity and spin canting in spin-orbit proximitized rhombohedral trilayer graphene (2024), arXiv:2408.10190 [cond-mat.mes-hall].

[28] J. Yang, X. Shi, S. Ye, C. Yoon, Z. Lu, V. Kakani, T. Han, J. Seo, L. Shi, K. Watanabe, T. Taniguchi, F. Zhang, and L. Ju, Diverse impacts of spin-orbit coupling on superconductivity in rhombohedral graphene (2024), arXiv:2408.09906 [cond-mat.supr-con].

[29] Y. Choi, Y. Choi, M. Valentini, C. L. Patterson, L. F. W. Holleis, O. I. Sheekey, H. Stoyanov, X. Cheng, T. Taniguchi, K. Watanabe, and A. F. Young, Electric field control of superconductivity and quantized anomalous hall effects in rhombohedral tetralayer graphene (2024), arXiv:2408.12584 [cond-mat.mes-hall].

[30] C. Huang, T. M. R. Wolf, W. Qin, N. Wei, I. V. Blinov, and A. H. MacDonald, Spin and orbital metallic magnetism in rhombohedral trilayer graphene, Phys. Rev. B **107**, L121405 (2023).

[31] A. Ghazaryan, T. Holder, M. Serbyn, and E. Berg, Unconventional superconductivity in systems with annular fermi surfaces: Application to rhombohedral trilayer graphene, Phys. Rev. Lett. **127**, 247001 (2021).

[32] A. Ghazaryan, T. Holder, E. Berg, and M. Serbyn, Multilayer graphenes as a platform for interaction-driven physics and topological superconductivity, Phys. Rev. B **107**, 104502 (2023).

[33] S. Chatterjee, T. Wang, E. Berg, and M. P. Zaletel, Intervalley coherent order and isospin fluctuation mediated superconductivity in rhombohedral trilayer graphene, Nature Communications **13**, 6013 (2022).

[34] Y.-Z. You and A. Vishwanath, Kohn-luttinger superconductivity and intervalley coherence in rhombohedral trilayer graphene, Phys. Rev. B **105**, 134524 (2022).

[35] A. L. Szabó and B. Roy, Metals, fractional metals, and superconductivity in rhombohedral trilayer graphene, Phys. Rev. B **105**, L081407 (2022).

[36] D.-C. Lu, T. Wang, S. Chatterjee, and Y.-Z. You, Correlated metals and unconventional superconductivity in rhombohedral trilayer graphene: A renormalization

group analysis, Phys. Rev. B **106**, 155115 (2022).
[37] W. Qin, C. Huang, T. Wolf, N. Wei, I. Blinov, and A. H. MacDonald, Functional renormalization group study of superconductivity in rhombohedral trilayer graphene, Phys. Rev. Lett. **130**, 146001 (2023).
[38] T. Cea, P. A. Pantaleón, V. o. T. Phong, and F. Guinea, Superconductivity from repulsive interactions in rhombohedral trilayer graphene: A kohn-luttinger-like mechanism, Phys. Rev. B **105**, 075432 (2022).
[39] P. A. Pantaleón, A. Jimeno-Pozo, H. Sainz-Cruz, V. Phong, T. Cea, and F. Guinea, Superconductivity and correlated phases in non-twisted bilayer and trilayer graphene, Nature Reviews Physics **5**, 304 (2023).
[40] Y.-Z. Chou, F. Wu, J. D. Sau, and S. Das Sarma, Acoustic-phonon-mediated superconductivity in moiréless graphene multilayers, Phys. Rev. B **106**, 024507 (2022).
[41] S. C. de la Barrera, S. Aronson, Z. Zheng, K. Watanabe, T. Taniguchi, Q. Ma, P. Jarillo-Herrero, and R. Ashoori, Cascade of isospin phase transitions in bernal-stacked bilayer graphene at zero magnetic field, Nature Physics **18**, 771 (2022).
[42] A. M. Seiler, F. R. Geisenhof, F. Winterer, K. Watanabe, T. Taniguchi, T. Xu, F. Zhang, and R. T. Weitz, Quantum cascade of correlated phases in trigonally warped bilayer graphene, Nature **608**, 298 (2022).
[43] Z. Dong, A. V. Chubukov, and L. Levitov, Transformer spin-triplet superconductivity at the onset of isospin order in bilayer graphene, Phys. Rev. B **107**, 174512 (2023).
[44] A. L. Szabó and B. Roy, Competing orders and cascade of degeneracy lifting in doped bernal bilayer graphene, Phys. Rev. B **105**, L201107 (2022).
[45] Y.-Z. Chou, F. Wu, J. D. Sau, and S. Das Sarma, Acoustic-phonon-mediated superconductivity in bernal bilayer graphene, Phys. Rev. B **105**, L100503 (2022).
[46] Y.-Z. Chou, F. Wu, and S. Das Sarma, Enhanced superconductivity through virtual tunneling in bernal bilayer graphene coupled to wse_2, Phys. Rev. B **106**, L180502 (2022).
[47] A. Jimeno-Pozo, H. Sainz-Cruz, T. Cea, P. A. Pantaleón, and F. Guinea, Superconductivity from electronic interactions and spin-orbit enhancement in bilayer and trilayer graphene, Phys. Rev. B **107**, L161106 (2023).
[48] T. Cea, Superconductivity induced by the intervalley coulomb scattering in a few layers of graphene, Phys. Rev. B **107**, L041111 (2023).
[49] J. B. Curtis, N. R. Poniatowski, Y. Xie, A. Yacoby, E. Demler, and P. Narang, Stabilizing fluctuating spin-triplet superconductivity in graphene via induced spin-orbit coupling, Phys. Rev. Lett. **130**, 196001 (2023).
[50] W. Kohn and J. M. Luttinger, New mechanism for superconductivity, Phys. Rev. Lett. **15**, 524 (1965).
[51] Y.-P. Lin and R. M. Nandkishore, Kohn-luttinger superconductivity on two orbital honeycomb lattice, Phys. Rev. B **98**, 214521 (2018).
[52] J. González and T. Stauber, Kohn-luttinger superconductivity in twisted bilayer graphene, Phys. Rev. Lett. **122**, 026801 (2019).
[53] A. Jahin and S.-Z. Lin, Enhanced kohn-luttinger topological superconductivity in bands with nontrivial geometry (2024), arXiv:2411.09664 [cond-mat.supr-con].
[54] Z. Li, X. Kuang, A. Jimeno-Pozo, H. Sainz-Cruz, Z. Zhan, S. Yuan, and F. Guinea, Charge fluctuations, phonons, and superconductivity in multilayer graphene, Phys. Rev. B **108**, 045404 (2023).
[55] E. McCann and V. I. Fal'ko, Landau-level degeneracy and quantum hall effect in a graphite bilayer, Phys. Rev. Lett. **96**, 086805 (2006).
[56] J. Jung and A. H. MacDonald, Accurate tight-binding models for the π bands of bilayer graphene, Phys. Rev. B **89**, 035405 (2014).
[57] In practice, we pick a UV cutoff of $0.025 \times (\pi/a)$ where a is the lattice constant of graphene.
[58] A. Jimeno-Pozo, H. Sainz-Cruz, T. Cea, P. A. Pantaleón, and F. Guinea, Private communication.
[59] G. Wagner, Y. H. Kwan, N. Bultinck, S. H. Simon, and S. A. Parameswaran, see supplementary material to this article for details of the single-particle Hamiltonian, the RPA calculation and the FRG equations..
[60] J. Polchinski, Renormalization and effective lagrangians, Nuclear Physics B **231**, 269 (1984).
[61] R. Shankar, Renormalization-group approach to interacting fermions, Rev. Mod. Phys. **66**, 129 (1994).
[62] W. Metzner, M. Salmhofer, C. Honerkamp, V. Meden, and K. Schönhammer, Functional renormalization group approach to correlated fermion systems, Rev. Mod. Phys. **84**, 299 (2012).
[63] C. Platt, W. Hanke, and R. Thomale, Functional renormalization group for multi-orbital fermi surface instabilities, Advances in Physics **62**, 453 (2013).
[64] M. Salmhofer, Renormalization in condensed matter: Fermionic systems – from mathematics to materials, Nuclear Physics B **941**, 868 (2019).
[65] N. Dupuis, L. Canet, A. Eichhorn, W. Metzner, J. Pawlowski, M. Tissier, and N. Wschebor, The nonperturbative functional renormalization group and its applications, Physics Reports **910**, 1 (2021).
[66] P. Kopietz, L. Bartosch, and F. Schütz, *Introduction to the Functional Renormalization Group* (Springer Berlin Heidelberg, 2010).
[67] D. M. Kennes, J. Lischner, and C. Karrasch, Strong correlations and $d + id$ superconductivity in twisted bilayer graphene, Phys. Rev. B **98**, 241407 (2018).
[68] L. Klebl, D. M. Kennes, and C. Honerkamp, Functional renormalization group for a large moiré unit cell, Phys. Rev. B **102**, 085109 (2020).
[69] Q.-K. Tang, L. Yang, D. Wang, F.-C. Zhang, and Q.-H. Wang, Spin-triplet f-wave pairing in twisted bilayer graphene near $\frac{1}{4}$-filling, Phys. Rev. B **99**, 094521 (2019).
[70] L. Classen, C. Honerkamp, and M. M. Scherer, Competing phases of interacting electrons on triangular lattices in moiré heterostructures, Phys. Rev. B **99**, 195120 (2019).
[71] C. Neumann, S. Reichardt, P. Venezuela, M. Drögeler, L. Banszerus, M. Schmitz, K. Watanabe, T. Taniguchi, F. Mauri, B. Beschoten, S. V. Rotkin, and C. Stampfer, Raman spectroscopy as probe of nanometre-scale strain variations in graphene, Nature Communications **6**, 8429 (2015).
[72] J. Martin, N. Akerman, G. Ulbricht, T. Lohmann, J. H. Smet, K. von Klitzing, and A. Yacoby, Observation of electron–hole puddles in graphene using a scanning single-electron transistor, Nature Physics **4**, 144 (2008).
[73] J. Xue, J. Sanchez-Yamagishi, D. Bulmash, P. Jacquod, A. Deshpande, K. Watanabe, T. Taniguchi, P. Jarillo-Herrero, and B. J. LeRoy, Scanning tunnelling microscopy and spectroscopy of ultra-flat graphene on hexagonal boron nitride, Nature Materials **10**, 282

(2011).
[74] S. Raghu and S. A. Kivelson, Superconductivity from repulsive interactions in the two-dimensional electron gas, Phys. Rev. B **83**, 094518 (2011).
[75] A. V. Chubukov, Kohn-luttinger effect and the instability of a two-dimensional repulsive fermi liquid at t=0, Phys. Rev. B **48**, 1097 (1993).
[76] P. O. Sukhachov, F. von Oppen, and L. I. Glazman, Andreev reflection in scanning tunneling spectroscopy of unconventional superconductors, Phys. Rev. Lett. **130**, 216002 (2023).
[77] E. Pangburn, L. Haurie, A. Crépieux, O. A. Awoga, N. Sedlmayr, A. M. Black-Schaffer, C. Pépin, and C. Bena, Superconductivity in monolayer and few-layer graphene. iii. impurity-induced subgap states and quasiparticle interference patterns, Phys. Rev. B **108**, 134516 (2023).
[78] G. Wagner, Y. H. Kwan, N. Bultinck, S. H. Simon, and S. A. Parameswaran, Global phase diagram of the normal state of twisted bilayer graphene, Phys. Rev. Lett. **128**, 156401 (2022).
[79] J. Kang, B. A. Bernevig, and O. Vafek, Cascades between light and heavy fermions in the normal state of magic-angle twisted bilayer graphene, Phys. Rev. Lett. **127**, 266402 (2021).
[80] A. S. Patri and T. Senthil, Strong correlations in abc-stacked trilayer graphene: Moiré is important, Phys. Rev. B **107**, 165122 (2023).
[81] Y. Xia, Z. Han, K. Watanabe, T. Taniguchi, J. Shan, and K. F. Mak, Superconductivity in twisted bilayer wse2, Nature 10.1038/s41586-024-08116-2 (2024).
[82] Y. Guo, J. Pack, J. Swann, L. Holtzman, M. Cothrine, K. Watanabe, T. Taniguchi, D. Mandrus, K. Barmak, J. Hone, A. J. Millis, A. N. Pasupathy, and C. R. Dean, Superconductivity in twisted bilayer wse_2 (2024), arXiv:2406.03418 [cond-mat.mes-hall].
[83] W. Qin, W.-X. Qiu, and F. Wu, Kohn-luttinger mechanism of superconductivity in twisted bilayer wse_2: Gate-tunable unconventional pairing symmetry (2024), arXiv:2409.16114 [cond-mat.supr-con].